

A small-scale dynamics model using unstructured meshes

Joanna Szmelter^a, Zhao Zhang^a, Piotr K. Smolarkiewicz^b

^a *Loughborough University, Leicestershire LE11 3TU, UK*

^b *European Centre for Medium-Range Weather Forecasts, Reading, RG2 9AX, UK*

ABSTRACT

The paper describes a limited area non-hydrostatic model operating on fully unstructured meshes with a collocated arrangement of flow variables. The model belongs to a non-oscillatory forward-in-time (NFT) class of solvers and combines the Multidimensional Positive Definite Advection Transport Algorithm (MPDATA) and a robust non-symmetric Krylov-subspace elliptic solver. It employs a finite volume spatial discretisation with edge-based data structure implemented on unstructured meshes that admit arbitrarily shaped cells. Numerical examples illustrate mesh flexibility offered by the proposed approach, including mesh adaptivity using MPDATA based error indicator.

1 Introduction

Atmospheric flows evince fluid motions ranging from dissipation scales as small as a fraction of a millimetre, to planetary scales of thousands of kilometres. For some problems, such as weather conditions in long winding valleys, tropical storms or hurricane forecasting, inadequacies in traditional structured mesh (grid) resolution may limit the accuracy attainable with available resources. In contrast, unstructured-meshes and mesh adaptivity offer flexibility that can address the increasing resolution requirements.

The paper describes an implementation of the three-dimensional, high-resolution, non-hydrostatic, limited area model for flexible fully unstructured meshes. The model derived in [15] exploits non-oscillatory control volume integrators for rotating stably-stratified flows that use a non-oscillatory forward-in-time (NFT) approach, analogous to that employed in the non-hydrostatic all-scale, multi-physics structured grid models reviewed in [7]. NFT labels a class of second-order-accurate two-time-level algorithms built on nonlinear advection techniques that suppress/reduce/control numerical oscillations characteristic of higher-order linear schemes; and it is meant to distinguish these algorithms from classical centered-in-time-and-space linear methods. The model admits several soundproof systems, including the classical incompressible Boussinesq [17], anelastic Lipps-Hemler [5, 6] and Durran pseudo-incompressible [1] partial differential equations. It utilises the non-oscillatory advection scheme MPDATA, derived for unstructured meshes from first principles in [11, 12]. The solution of the elliptic Poisson equation, implied by the soundproof mass-continuity constraint, employs a robust non-symmetric Krylov-subspace solver detailed in [14]. In [15], the model performance was demonstrated on dual meshes constructed from primary prismatic meshes with triangular and quadrilateral bases. This paper extends the model applicability to dual meshes built on primary tetrahedral meshes.

The two-dimensional option of the non-hydrostatic NFT MPDATA scheme [20, 14] verified the accuracy of the two-dimensional edge-based approach using benchmarks from both analytic and laboratory results, and comparing unstructured mesh results to the corresponding structured grid model results for simulations of non-hydrostatic mountain waves at weak and strong background stratifications with linear and nonlinear flow response, respectively. Herein, we employ the two dimensional non-hydrostatic model option to demonstrate the flexibility of unstructured meshes in the context of static adaptive mesh

refinement. An a posteriori error indicator that drives the mesh refinement arises from the properties of MPDATA [18].

Our developments of the non-hydrostatic modeling using unstructured-mesh NFT framework have so far addressed mesoscale orographic flows, with a range of internal gravity wave phenomena in two and three spatial dimensions [20, 14, 15]. Furthermore, LES of convective planetary boundary layer [15] demonstrated suitability of the approach for accurate simulation of high-Reynolds-number thermal convection, with stochastic flow realisations but predictable integral characteristics. The hydrostatic modeling has been addressed in the earlier NFT MPDATA developments. It included generalisations of shallow-water equations to global spherical geometry [19], and a class of three dimensional global models [19, 20] that employ a classical geospherical reference frame, with the governing equations cast in the latitude-longitude surface-based coordinates. Noteworthy, notorious issues associated with meridians convergence near the poles were resolved by exploiting the flexibility of unstructured mesh discretisation. A corresponding unstructured mesh finite volume NFT framework was also formulated for modeling all-speed engineering flows [18, 13]. The numerical results presented here capture the key aspects of canonical flow problems for limited area gravity wave dynamics and flows over complex terrain.

2 Numerical algorithm

2.1 Non-oscillatory forward in time integration

The numerical solutions presented in the paper are obtained by integrating either the incompressible Boussinesq or the anelastic Lipps-Hemler PDEs. In both cases, the governing conservation laws of mass, momentum and thermodynamic properties can be compactly written as

$$\begin{aligned} \nabla \cdot (\mathbf{V}\rho_o) &= 0, \\ \frac{\partial \rho_o V^I}{\partial t} + \nabla \cdot (\mathbf{V}\rho_o V^I) &= \rho_o \left(-\frac{\partial \tilde{p}}{\partial x^I} + g \frac{\theta'}{\theta_o} \delta_{I3} \right), \\ \frac{\partial \rho_o \theta}{\partial t} + \nabla \cdot (\mathbf{V}\rho_o \theta) &= 0. \end{aligned} \quad (1)$$

Here, ρ , θ and p denote the density, potential temperature and pressure, and the normalised pressure perturbation $\tilde{p} \equiv p'/\rho_o$. For $I = 1, 2$, the velocity components refer to the horizontal directions $x^1 \equiv x$, $x^2 \equiv y$ with $V^1 \equiv u$, $V^2 \equiv v$; whereas in the vertical $I = 3$ with $x^3 \equiv z$ and $V^3 \equiv w$. Subscripts $_o$ denote the static reference state, while primes denote perturbations with respect to a hydrostatically balanced ambient state. In the Boussinesq case, constant ρ_o and θ_o imply $p_o \propto z$; whereas in the anelastic case vertical profiles $\rho_o(z)$ and $p_o(z)$ are defined in terms of a constant stratification $S_o = N^2/g$ — so $\theta_o \propto \exp(S_o z)$ — where $g (= 9.81 \text{ ms}^{-2})$ and N denote the gravitational acceleration and the buoyancy frequency, respectively. In examples discussed in this paper the ambient states assume constant wind U and thermodynamic profiles defined by S_o according to the hydrostatic balance of the governing PDEs.

For the construction of numerical solution to the momentum and the potential temperature equation in (1), the generic NFT template algorithm is applied

$$\begin{aligned} \forall_{i,n} \quad \Phi_i^{n+1} &= \mathcal{A}_i(\Phi^n + 0.5\delta t R^n, \mathcal{V}^{n+1/2}, \rho_o) + 0.5\delta t R_i^{n+1} \\ &\equiv \mathcal{A}_i(\tilde{\Phi}, \mathcal{V}^{n+1/2}, \rho_o) + 0.5\delta t R_i^{n+1} \\ &\equiv \hat{\Phi}_i + 0.5\delta t R_i^{n+1}, \end{aligned} \quad (2)$$

with Φ symbolising a dependent flow variable V^I or θ and R denoting the ratio of the associated rhs in (1) to ρ_o . Indices n and i have their usual meaning of the temporal and spatial positions. The operator \mathcal{A}

is a shorthand for the edge-based MPDATA [12], and it already accounts for a division of conservative variables $\rho_o \Phi$ by ρ_o . The $\mathcal{V}^{n+1/2}$ argument of \mathcal{A} denotes a $\mathcal{O}(\delta t^2)$ estimate of $\rho_o \mathbf{V}$ at $t + 0.5\delta t$; whereas R^{n+1} is a second-order-accurate finite volume representation of R ; see [16] in the same volume for a discussion.

In its simplest form, the solution commences with the linear extrapolation of advective mass flux

$$\mathcal{V}_i^{n+1/2} = 1.5\mathcal{V}_i^n - 0.5\mathcal{V}_i^{n-1}, \quad (3)$$

followed by the computation of auxiliary variables

$$\begin{aligned} \tilde{\mathbf{V}}_i &= \mathbf{V}_i^n - 0.5\delta t \left(\nabla \tilde{p} - g \frac{\theta'}{\theta_o} \mathbf{k} \right)_i^n, \\ \tilde{\theta}_i &= \theta_i^n, \end{aligned} \quad (4)$$

and their subsequent MPDATA transport supplying $\hat{\mathbf{V}}$ and $\hat{\theta}$ in (2); here $\mathbf{k} = \nabla_z$ denotes the unit vector in the vertical. For inviscid adiabatic flows, $\hat{\theta} \equiv \theta^{n+1}$ completes the solution of the potential temperature equation, thus providing an $\mathcal{O}(\delta t^3)$ estimate of the buoyancy force on the rhs of the vertical momentum equation. In consequence, in the corresponding realizations of (2) for the momentum equation,

$$\mathbf{V}_i^{n+1} = \hat{\mathbf{V}}_i - 0.5\delta t \left(\nabla \tilde{p} - g \frac{\theta'}{\theta_o} \mathbf{k} \right)_i^{n+1}, \quad (5)$$

the components of the pressure gradient $\nabla \tilde{p}^{n+1}$ are the only unknowns on the rhs. The discrete elliptic Poisson problem for pressure can be now formed by applying the discrete divergence operator to $\rho_o \times (5)$ and noting that $\nabla_i \cdot (\rho_o \mathbf{V})^{n+1}$ must vanish on the left-hand-side due to the continuity constraint in (1):

$$\forall_i \quad \nabla_i \cdot \rho_o \left(\hat{\mathbf{V}} - 0.5\delta t \nabla \tilde{p}^{n+1} \right) = 0, \quad (6)$$

where $\hat{\hat{\mathbf{V}}} = \hat{\mathbf{V}} + 0.5\delta t g (\theta'/\theta_o)^{n+1} \mathbf{k}$ forms the explicit part of the problem. The resulting system (6) is solved to a specified tolerance using the preconditioned generalized conjugate residual algorithm; cf. [14]. Given the solution to (6), combining the updated buoyancy and pressure-gradient components on the rhs of (5) completes the solution. For more elaborate semi-implicit NFT algorithms implemented on structured meshes that account for implicit representations of the buoyancy and Coriolis forces see [16] in the same volume.

The spatial discretisation assumed in the template algorithm (2) uses the edge-based median-dual finite volume approach [12] integrating the generic physical form of the governing PDE over arbitrarily-shaped cells. A schematic of the edge-based data structure for an arbitrary hybrid mesh on a 2D plane is shown in Figure 1. The median-dual finite volume approach constructs the control volume associated with the vertex i by joining the centres of polygonal mesh cells encompassing the vertex i and midpoints of edges originating in the vertex i , Figure 1. Having defined the mesh in planar geometry, all geometric elements such as cell volume, cell face area, and normals are evaluated from vector calculus. All solution variables are collocated in the vertexes. The construction of a dual mesh in three dimensions is similar. Figure 2 illustrates a control volume cell face associated with the edge, formed by joining barycenters of the primary mesh and centres of primary mesh element faces.

2.2 MPDATA error indicator for mesh adaptivity

The finite volume discretisation with the edge-based data structure is well suited for investigating refined mesh-point distributions. In particular, this includes a flexible use of mesh adaptivity techniques, for

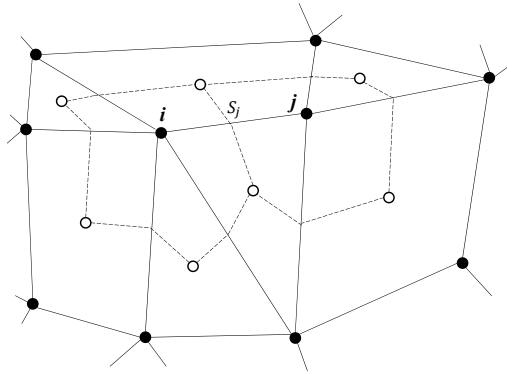


Figure 1: The edge-based, median-dual approach in 2D. The edge connecting vertices i and j of the primary polygonal mesh pierces, precisely in its middle, the face S_j shared by computational dual cells surrounding vertices i and j ; open circles represent barycenters of the primary mesh, while solid and dashed lines mark primary and dual meshes, respectively.

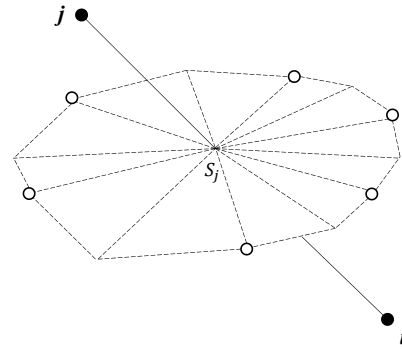


Figure 2: The edge-based median-dual approach in 3D. The edge connecting vertices i and j of the primary mesh pierces (at the edge center) the face S_j of a computational (dual) cell surrounding vertex i ; open circles represent barycenters of polyhedral cells surrounding the edge. Dashed lines mark a fragment of the dual mesh; cf. Figure 1.

which an explicit analytic form of the error estimator naturally arising from MPDATA [18] can be employed.

MPDATA relies on the iterative application of the upwind scheme, where subsequent iterations compensate for the implicit viscosity of the preceding steps. In MPDATA the first- and second-order solutions as well as the leading error are known explicitly. The analytic forms of the truncation errors for the edge-based formulation of MPDATA can be found in [12]. Having error forms and measures available naturally dictates refinement indicators, akin to the Richardson extrapolation, that take advantage of the property that a more accurate solution is obtained from every subsequent upwind iteration.

The subsequent solution update can therefore be written in brief as

$$\tilde{\Phi}_i^p = \tilde{\Phi}_i^{p-1} - \frac{\delta t}{\vartheta_i} RHS_i^{p-1}; \quad p = 1, \dots, IORD. \quad (7)$$

Here p numbers upwind iterations in MPDATA, initiated with values from the previous time step n , $\tilde{\Phi}^0 \equiv \tilde{\Phi}^n$, and ϑ_i is a volume (area in 2D) of the i th dual cell. At the end of the upwind iterations $\tilde{\Phi}^{IORD} = \tilde{\Phi}^{n+1}$. Thus, $\tilde{\Phi}^1$ is the first-order accurate upwind solution. While $(\delta t / \vartheta) RHS^0$ represents the integral (first-order accurate) of the divergence of the convective flux, $(\delta t / \vartheta) RHS^1$ is a first-order approximation to the leading truncation error of the solution integral.

There is no unique way to devise a practical error indicator. For example, setting $\tilde{\Phi} \equiv \theta$ gives the basic refinement indicator defined for all edges associated with i th node as

$$\eta_{ij} = \frac{|RHS_i^p - RHS_j^p|}{\text{Max}_{i=1, \dots, \mathcal{N}} |RHS_i^p|}; \quad j = 1, l(i), \quad (8)$$

where \mathcal{N} denotes total number of nodes. In terms of residual errors, for $p = 2$ the residual error is based on comparing the first- and second-accurate solutions, while for $p = 3$ it is constructed from

the second- and (nearly) third-order solutions. In practice, however, the indicator (8) acts similarly for either two or three upwind passes in MPDATA [18], consistently with observation that the phase errors of MPDATA solutions are insensitive to p . Therefore, the indicator obtained for $p = 2$ is typically used in applications. Furthermore, in all examples presented here we use MPDATA infinite gauge option for which $p = 2$ by design; cf. section 5.1 in [12].

3 Results

3.1 Stratified Boussinesq Flow Past a Steep Isolated Hill

The canonical stratified flow past an axially-symmetric cosine hill [3, 2, 10] is adopted to evaluate the performance of the non-hydrostatic NFT MPDATA finite volume edge-based scheme. In [15], the simulation of this problem was computed on dual meshes derived from structured and prismatic primary meshes. Here, the validation of the scheme extends previous studies to include tetrahedral primary meshes.

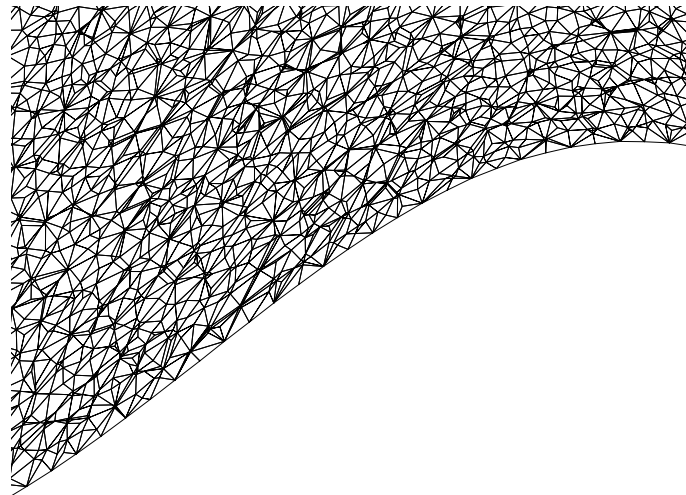


Figure 3: A xz cross-section through the central, $y = 0$, plane near the hill. Nearby mesh points are projected on the cross-section for visualisation. The primary mesh is fully unstructured and consists of tetrahedral elements only. The computation is conducted on the dual mesh built from the primary mesh.

A hill with height $h(x, y) = h_0 \cos^2(\pi r/2L)$ if $r = (x^2 + y^2)^{1/2} \leq L$ and $h = 0$ otherwise is placed at the bottom of computational domain at its centre. The domain size is $5L \times 4L \times 2L$ in x , y and z directions, respectively, where $L = 3000$ m and $h_0 = 1500$ m. A fully unstructured primary mesh consisting of tetrahedral elements was generated in the domain using an uniform background point spacing of $\delta x = \delta y = \delta z = 120$ m. Figure 3 shows a representative fragment of the tetrahedral mesh in cross-section plane $y=0$ near the hill. Nearby mesh points are projected on the cross-section for ease of illustration. The total number of points in the mesh is 1945090. The computational dual mesh consists of polyhedra built by connecting barycenters of the tetrahedral elements, centres of the elements' faces and middle points of edges.

The constant environmental wind is specified at $U = 5 \text{ ms}^{-1}$, and a constant buoyancy frequency is $N = 10^{-2} \text{ s}^{-1}$. The potential temperature of the reference state is $\theta_0 = 300\text{K}$. With the specified hill geometry, the ambient conditions result in a low Froude number, $Fr = U/Nh_0 = 1/3$, flow. The problem is essentially non-hydrostatic and can be compared to experimental results given in [3], with $h_0/L \sim$

$\mathcal{O}(1)$ and Rossby number $Ro = U/Lf_z \nearrow \infty$.

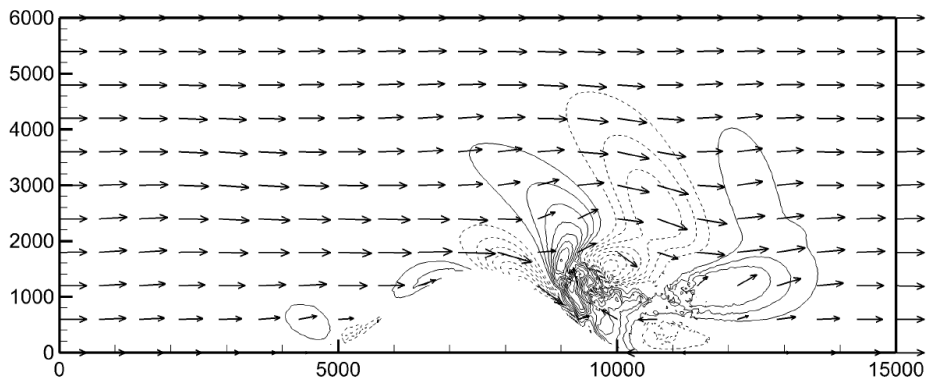


Figure 4: Contours of vertical velocity in central xz cross section ($y = 0$). The contour interval is 0.5 ms^{-1} , and $Fr = 1/3$. The result is obtained after two advective time scales $T = L/U$. Positive and negative contours are presented with solid and dashed lines, respectively; the zero contours are not displayed. The velocity vectors are interpolated from the unstructured mesh to a Cartesian mesh.

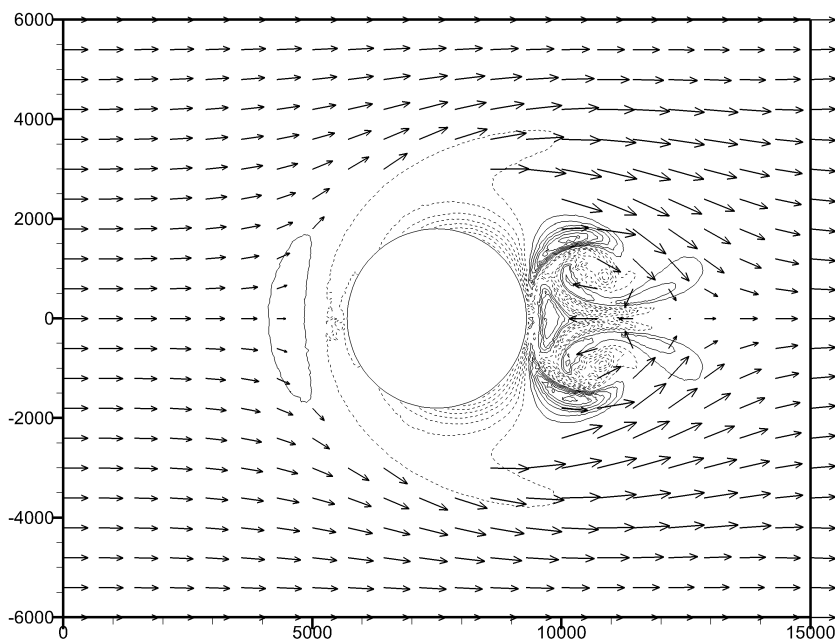


Figure 5: As in Figure 4, but for the contours of vertical velocity at $z = 500 \text{ m}$ horizontal cross-section.

The results are obtained after two advective time scales $T = L/U$, at $t = 1200\text{s}$, when the main features of the solution are already established. The initial condition is provided by the solution of the potential flow problem, with a gradient of the potential perturbation imposed on the ambient wind. While the boundary conditions are rigid in x , y and z , the gravity-wave absorbers near the upper and lateral stream-wise boundaries attenuate the solution toward ambient profiles with absorbing coefficient increasing linearly from zero at the distance $L/2$ from the boundary to 150^{-1} s^{-1} at the boundary.

The flow patterns displayed in figures 4, 5 and 6 are computed with the incompressible Boussinesq option of the scheme and show key features of a non-rotating low Froude number flow, including the characteristic separation and reversal of the lower upwind stream, and the formation of intense vertically-oriented vortices on the lee side of the hill [3, 10, 2], with the flow aloft transitioning to the linear gravity

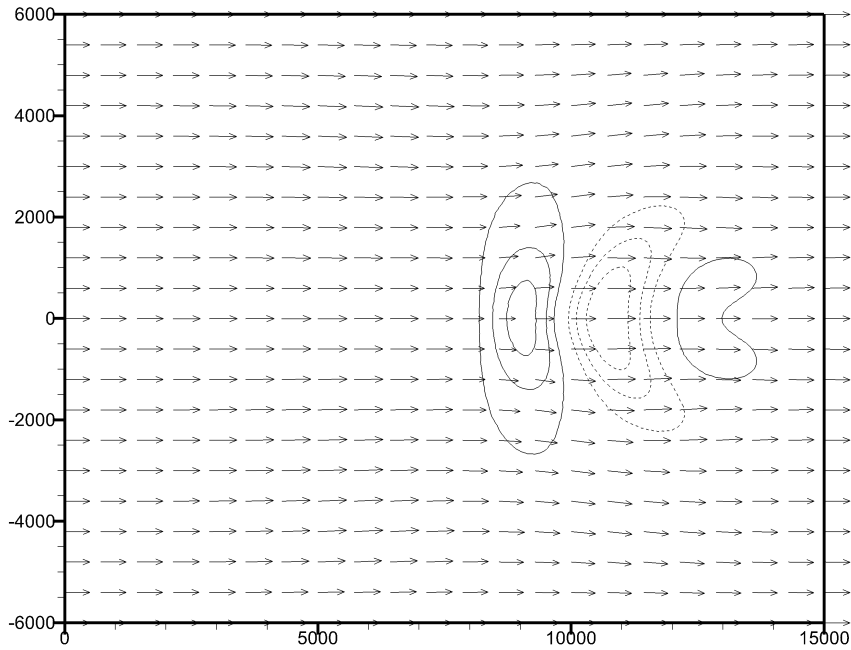


Figure 6: AS in Figure 5 but at the $z = 2500$ m horizontal cross-section.

wave response [9]. In Figure 4, in the central xz cross-section at $y = 0$, a turbulent wake is formed in the lee-side of the hill and characteristic gravity waves response is visible above the wake. This result matches closely the reference solution obtained on structured and prismatic meshes (upper panels in Figures 6 and 8 in [15]). Figure 5, in xy cross-section at $z = 500$ m, presents a pair of eddies behind the hill, showing the intrinsic three-dimensionality of the lee-side flow. The reason of this flow structure is that the incoming flow up to $z_c \approx (1 - Fr)h_0$ is forced to deflect and split close to the hill as it lacks sufficient kinetic energy to go over the hill. Figure 6 shows the gravity-wave responses aloft on the xy cross-section $z = 2500$ m. The two horizontal flow patterns also compare well with the reference results in [15]. The statistics of the results are presented in Table 1. The units of the three velocity components and potential temperature are ms^{-1} and K. The statistics of Θ' are converted to the vertical displacements of isentropes using a crude approximation

$$\eta_z \approx -\theta' \frac{g}{N^2 \theta_0} \approx -333 \theta' \text{ m} . \quad (9)$$

The extrema of variable fluctuations about the ambient state are taken over the entire computational domain. The irregularity of the mesh is taken into account when calculating the averages and standard deviations of the fluctuations. With ϑ_i denoting the cell volume surrounding mesh point i , the average values $\overline{\phi'}$ are calculated according to

$$\overline{\phi'} = \frac{\sum_{i=1}^n (\phi'_i \vartheta_i)}{\sum_{i=1}^n \vartheta_i} , \quad (10)$$

and the corresponding standard deviations $\sigma_{\phi'}$ are calculated as

$$\sigma_{\phi'} = \frac{\sum_{i=1}^n ((\phi'_i - \overline{\phi'})^2 \vartheta_i)}{\sum_{i=1}^n \vartheta_i} . \quad (11)$$

The results summarized in the table are obtained on a fully unstructured mesh with the implicit Boussinesq model. They are consistent with those in Table 2 of [15], obtained with anelastic equations integrated on an unstructured prismatic mesh and a structured grid.

Variable	Maximum	Minimum	Average	Standard Deviation
u'	3.51	-11.39	0.06	0.76
v'	8.04	-8.48	4.7×10^{-6}	0.47
w'	5.35	-4.80	-1.02×10^{-4}	0.36
Θ'	2.85	-1.48	-4.7×10^{-3}	0.204
η'	-949	493	1.57	66.6

Table 1: Fluctuation's statistics on a fully unstructured mesh

3.2 Orographically-forced atmospheric gravity waves

The benchmark problem of Schär et al [8] is considered next to demonstrate the implementation of static mesh adaptivity within the unstructured mesh edge-based finite volume spatial discretisation framework. The problem consists of an anelastic flow past a terrain profile under stably stratified atmospheric conditions, as described in [21] while following [8, 4]. The terrain profile is given by

$$z_s(x) = z_{s0} \exp\left(\frac{-x^2}{a^2}\right) \cos^2\left(\frac{\pi x}{\lambda}\right) \quad (12)$$

with $z_{s0} = 0.25$ km, $a = 5$ km and $\lambda = 4$ km. The buoyancy frequency $N = 0.01s^{-1}$; the ambient wind profile is $U = 10$ ms $^{-1}$; the computational domain is 70×21 km and the simulation time is 5 hours. The upper 11 km of the model domain is designated as an absorbing layer, to simulate an infinite atmosphere and to suppress spurious wave reflection from the upper rigid-lid. Lateral absorbers extend for 10 km away from the boundaries.

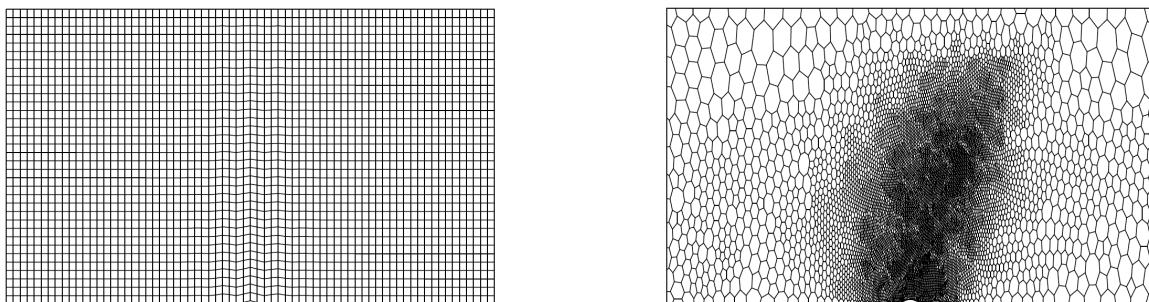


Figure 7: Coarse structured mesh and refined unstructured mesh

The solution of Lipps and Hemler anelastic system of governing equations [5, 6] is obtained using a semi-implicit extension [14] of the basic NFT MPDATA model outlined in section 2.1. The flow and geometry parameters in [8] are chosen to illustrate a bifurcation into a qualitatively incorrect solution for a specific arrangement of a sigma class of the terrain following transformation which is especially pronounced for solutions obtained on coarse meshes. The initial solution obtained in this work uses a purposely coarse 81×46 structured mesh shown in the left panel of Figure 7, with the resulting $\delta x = 875$ m and $\delta z \approx 467$ m, respectively, 1.75 and 1.5 times coarser than the increments used in the earlier works. The mesh conforms to the geometry of terrain and is constructed to mimic the Gal-Chen and Somerville terrain-following coordinates [21], but the solution is obtained in a physical space without a need for a transformation. The resulting vertical velocity contours given in the left panel of

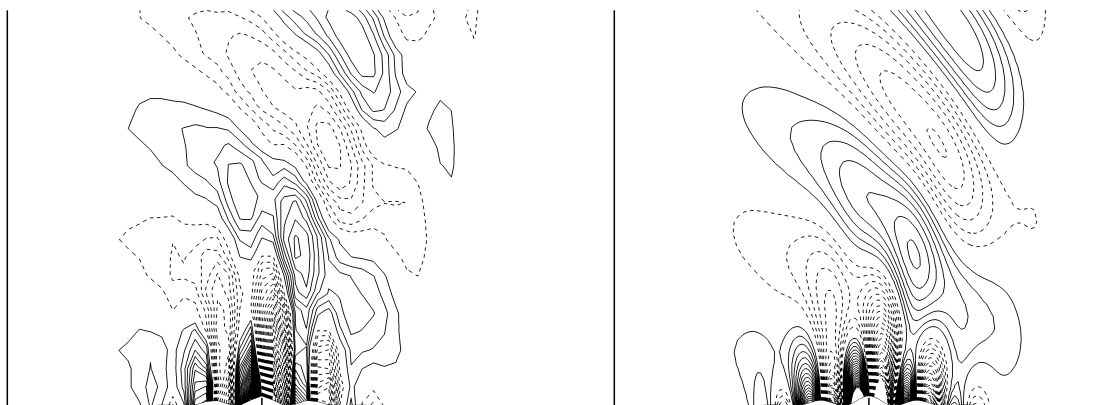


Figure 8: Vertical velocity of the flow past the terrain profile after 5 h of simulation when the steady state has been reached on coarser and finer meshes. The contour interval is 0.05 ms^{-1} and zero contour is not shown.

Figure 8 show much weaker spurious features than those reported in [8]. However, the coarse mesh solution carries sufficient information for the purpose of an adaptive error estimation.

The improved computational mesh is generated by a static mesh adaptivity utilising the initial solution obtained from the coarse mesh which provides input into the error estimator (8). The normalised error allows to specify a desired background spacing which in turn permits a generation of refined mesh. The advancing front technique is employed here for generating a new primary triangular mesh for which the corresponding dual mesh is shown in the right panel of Figure 7. As anticipated, the areas of finer mesh are present where the topography changes more rapidly and in the main wave train. In contrast, the mesh coarsens in the areas of smooth flow and absorbing boundaries. Figure 8 shows the corresponding vertical velocity contours obtained with the adapted mesh. The new solution is in agreement with the reference solution [8], and other published results [21], however it is obtained on a mesh containing 8662 nodes, as oppose to 10,011 employed in [21].

Notably, although the initial solution in this study was obtained on a coarse structured mesh, the proposed adaptivity procedure is flexible and can analogously be used with the initial solution obtained from the coarse mesh built on a base of a triangular primary mesh.

4 Remarks

An outline of a study exploring the applicability and flexibility of the finite volume discretisation operating on fully unstructured and adaptive meshes with the efficient edge-based data structure is presented. The numerical results illustrate the performance and potential of such meshes for simulating flows past complex terrain.

The successful validation of a limited area non-hydrostatic NFT MPDATA atmospheric model is further extended to meshes constructed from the irregular tetrahedral primary grids. The presented results confirm that the approach performs well for arbitrary shaped meshes. Furthermore, the results match the accuracy attainable on Cartesian grids with a similar spatial resolution.

An illustration of the static adaptivity provides an example of the potential for an automated generation of meshes with nodes distribution optimised for the problem at hand.

Acknowledgments:

The authors acknowledge support by the NERC/G004358 award and funding received from the European Research Council under the European Union's Seventh Framework Programme (FP7/2012/ERC Grant agreement no. 320375).

References

- [1] D.R. Durran, Improving the anelastic approximation, *J. Atmos. Sci.* 46 (1989) 1453-1461.
- [2] C.C. Epifanio, R. Rotunno, The dynamics of orographic wake formation in flows with upstream blocking, *J. Atmos. Sci.* 62 (2005) 3127–3150.
- [3] C.R. Hunt, W.H. Snyder, Experiments on stably and neutrally stratified flow over a model three-dimensional hill, *J. Fluid Mech.* 96 (1980) 671–704.
- [4] J.B. Klemp, W.C. Skamarock, O. Fuhrer, Numerical consistency of metric terms in terrain-following coordinates, *Month. Weather Rev.* 131 (2003) 1229–1239.
- [5] F.B. Lipps, R.S. Hemler, A scale analysis of deep moist convection and some related numerical calculations, *J. Atmos. Sci.* 39 (1982) 2192–2210.
- [6] F.B. Lipps, On the anelastic approximation for deep convection, *J. Atmos. Sci.* 47 (1990) 1794-1798.
- [7] J.M. Prusa, P.K. Smolarkiewicz, A.A. Wyszogrodzki, EULAG, a computational model for multi-scale flows, *Comput. Fluids* 37 (2008) 1193-1207
- [8] C. Schär, D. Leuenberger, O. Fuhrer, D. Lüthi, C. Girard, A new terrain-following vertical coordinate formulation for atmospheric prediction models, *Month. Weather Rev.* 130 (2002) 2459-2480.
- [9] R.B. Smith, Linear theory of hydrostatic flow over an isolated mountain in isosteric coordinates, *J. Atmos. Sci.* 45 (1988) 3887-3896.
- [10] P.K. Smolarkiewicz, R. Rotunno, Low Froude number flow past three-dimensional obstacles. Part I: Baroclinically generated lee vortices, *J. Atmos. Sci.* 46 (1989) 1154–1164.
- [11] P.K. Smolarkiewicz, J. Szmelter, Multidimensional positive definite advection transport algorithm (MPDATA) : an edge-based unstructured-data formulation, *Int. J. Numer. Meth. Fluids* 47 (2005) 1293-1299.
- [12] P.K. Smolarkiewicz, J. Szmelter, MPDATA: An Edge-Based Unstructured-Grid Formulation, *J. Comput. Phys.* 206 (2005) 624-649.
- [13] P.K. Smolarkiewicz, J. Szmelter, Iterated upwind schemes for gas dynamics, *J. Comput. Phys.* 228 (2009) 33–54.
- [14] P.K. Smolarkiewicz, J. Szmelter, A nonhydrostatic unstructured-mesh soundproof model for simulation of internal gravity waves, *Acta Geophysica* 59 (2011) 1109–1134.
- [15] P.K. Smolarkiewicz, J. Szmelter, A.A. Wyszogrodzki, An unstructured-mesh atmospheric model for nonhydrostatic dynamics, *J. Comput. Phys.* 254 (2013) 184–199.
- [16] P.K. Smolarkiewicz, C. Kühnlein, N.P. Wedi, A unified framework for integrating soundproof and compressible equations of all-scale atmospheric dynamics, *ibid.*

- [17] EA Spiegel, G. Veronis, On the Boussinesq approximation for compressible fluid, *Astrophys. J.* 131 (1960) 442–447.
- [18] J. Szmelter, P.K. Smolarkiewicz, MPDATA error estimator for mesh adaptivity, *Int. J. Numer. Meth. Fluids* 50 (2006) 1269-1293.
- [19] J. Szmelter, P.K. Smolarkiewicz, An edge-based unstructured mesh discretisation in geospherical framework, *J. Comput. Phys.* 229 (2010) 4980-4995.
- [20] J. Szmelter, P.K. Smolarkiewicz, An edge-based unstructured mesh framework for atmospheric flows, *Comput. Fluids.* 46 (2011) 455-460.
- [21] N.P. Wedi, P.K. Smolarkiewicz, Extending Gal-Chen and Somerville terrain-following coordinate transformation on time dependent curvilinear boundaries, *J. Comput. Phys.* 193 (2004) 1–20.

